JGR Space Physics

RESEARCH ARTICLE
10.1029/2023JA032328

Key Points:

- We use the ANGIE3D hybrid codes to simulate the interaction of four solar wind discontinuities with the bow shock
- The characteristics of foreshock transients observed by THEMIS D match the predictions of the hybrid simulation well
- The simulation also predicts the plasma and magnetic field variations observed during a magnetosheath cavity and a brief magnetopause entry

Correspondence to:
S. H. Lee,
leesh@cua.edu

Citation:
Lee, S. H., Sibeck, D. G., Wang, X., Lin, Y., Angelopoulos, V., Giles, B. L., et al. (2024). Cross-comparison of observations with the predictions of global hybrid simulations for multiple IMF discontinuities impacting the bow shock and magnetosheath. *Journal of Geophysical Research: Space Physics*, *129*, e2023JA032328. https://doi.org/10.1029/2023JA032328

Received 1 DEC 2023
Accepted 27 MAR 2024

Cross-Comparison of Observations With the Predictions of Global Hybrid Simulations for Multiple IMF Discontinuities Impacting the Bow Shock and Magnetosheath

S. H. Lee[1,2], D. G. Sibeck[2], X. Wang[3], Y. Lin[3], V. Angelopoulos[4], B. L. Giles[2], R. B. Torbert[5], C. T. Russell[4], H. Wei[4], and J. L. Burch[6]

[1]Catholic University of America, Washington, DC, USA, [2]NASA Goddard Space Flight Center, Greenbelt, MD, USA, [3]Physics Department, Auburn University, Auburn, AL, USA, [4]Department of Earth, Planetary, and Space Sciences, Institute of Geophysics and Planetary Physics, University of California, Los Angeles, Los Angeles, CA, USA, [5]Department of Physics, University of New Hampshire, Durham, NH, USA, [6]Southwest Research Institute, San Antonio, TX, USA

Abstract We use the three-dimensional (3-D) global hybrid code ANGIE3D to simulate the interaction of four solar wind tangential discontinuities (TDs) observed by ARTEMIS P1 from 0740 UT to 0800 UT on 28 December 2019 with the bow shock, magnetosheath, and magnetosphere. We demonstrate how the four discontinuities produce foreshock transients, a magnetosheath cavity-like structure, and a brief magnetopause crossing observed by THEMIS and MMS spacecraft from 0800 UT to 0830 UT. THEMIS D observed entries into foreshock transients exhibiting low density, low magnetic field strength, and high temperature cores bounded by compressional regions with high densities and high magnetic field strengths. The MMS spacecraft observed cavities with strongly depressed magnetic field strengths and highly deflected velocity in the magnetosheath downstream from the foreshock. Dawnside THEMIS A magnetosheath observations indicate a brief magnetosphere entry exhibiting enhanced magnetic field strength, low density, and decreased and deflected velocity (sunward flow). The solar wind inputs into the 3-D hybrid simulations resemble those seen by ARTEMIS. We simulate the interaction of four oblique TDs with properties similar to those in the observation. We place virtual spacecraft at the locations where observations were made. The hybrid simulations predict similar characteristics of the foreshock transients, a magnetosheath cavity, and a magnetopause crossing with characteristics similar to those observed by the multi-spacecraft observations. The detailed and successful comparison of the interaction involving multiple TDs will be presented.

1. Introduction

The Earth's foreshock is the solar wind region upstream from the Earth's magnetosphere that is magnetically connected to the bow shock and filled with backstreaming suprathermal particles reflected from and energized by encounters with the bow shock and encounters with plasma waves (Eastwood et al., 2005). Transient structures are common in the foreshock (Zhang & Zong, 2020; Zhang et al., 2022). Some of them are generated by the kinetic interaction of suprathermal ions with an interplanetary magnetic field (IMF) discontinuity, such as hot flow anomalies (HFAs, Schwartz et al., 1985) and foreshock bubbles (FBs, Omidi et al., 2010; Turner et al., 2013). Some, like foreshock cavities, from between pairs of discontinuities (Sibeck et al., 2002), while others form without an IMF discontinuity, such as spontaneous hot flow anomalies (SHFAs, Omidi et al., 2013; Zhang et al., 2013), foreshock cavitons (Blanco-Cano et al., 2011), and diamagnetic cavities (Lin, 2003; Lin & Wang, 2005). When a foreshock transient encounters the bow shock, its tenuous core of low dynamic pressure can cause the deformation of the local bow shock. These deformations can further disturb the magnetopause and generate field-aligned currents and ultra-low frequency (ULF) waves in the magnetosphere and trigger aurora brightenings (Archer et al., 2014, 2015; Shen et al., 2018; Sibeck et al., 1999; Turner et al., 2011; B. Wang et al., 2018; Zhang et al., 2022; Zhao et al., 2017).

Guo et al. (2020) compared the four Magnetospheric Multiscale (MMS; Burch et al., 2016) observations of a dayside magnetopause reconnection event with results from a 3-D global hybrid simulation. They showed that the formation and global distribution of the reconnection X-lines and the structure of the simulated reconnection were consistent with the MMS observations. Lee et al. (2021) compared multi-point observations of foreshock bubbles with results from a 2.5-D (2-D in space and 3-D in currents and electromagnetic fields) global hybrid simulation. The MMS spacecraft observed a series of discontinuities. Two out of five discontinuities generated foreshock

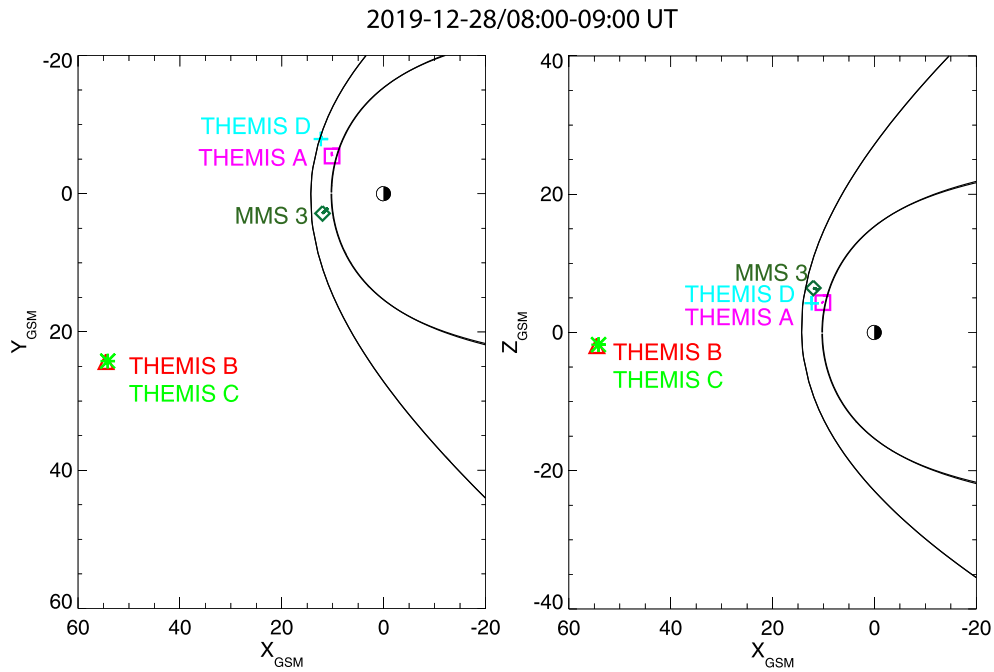

Figure 1. The positions of THEMIS A–E and MMS in the XY and XZ planes in GSM coordinates from 08:00 UT to 09:00 UT on 28 December 2019. The two black curves represent the locations of the bow shock and the magnetopause determined by the Fairfield model (Fairfield, 1971) and Shue model (Shue et al., 1997), respectively. The positions of three THEMIS probes and two ARTEMIS probes are marked by five different symbols.

bubbles. Lee et al. (2021) reported that MMS observations of the two fully developed foreshock bubbles were consistent with model predictions. While foreshock transients have been studied by 2-D (Lin, 1997, 2002; Omidi & Sibeck, 2007; Omidi et al., 2010, 2013) and 3-D (Lin et al., 2022; C.-P. Wang et al., 2020, 2021a, 2021b) global hybrid simulations, there are fewer studies on the impact of solar wind discontinuities, and their detailed structures in the magnetosphere have not been compared with results of 3-D global hybrid simulation. The goal of the present study is to investigate the effect of solar wind discontinuities as they pass by the magnetosphere such as foreshock transients, a magnetosheath cavity, and a brief magnetopause crossing as observed by the MMS and THEMIS spacecraft for comparison with results from a 3-D global hybrid simulation.

2. Observations: Event Overview

All data used in this paper are from the five-satellite Time History of Events and Macroscale Interactions During Substorms (THEMIS) mission (Angelopoulos, 2008; Sibeck et al., 2008) and four Magnetospheric Multiscale (MMS) satellites (MMS3; Burch et al., 2016). Each spinning THEMIS satellite (3 s spin period) is equipped with a fluxgate magnetometer (FGM; Auster et al., 2008), an electric field instrument (Bonnell et al., 2008), and an ion and electron electrostatic analyzer (ESA; McFadden et al., 2008). Two ARTEMIS probes (P1 and P2; Angelopoulos, 2011), part of the THEMIS mission, were moved to lunar orbits in 2010. ARTEMIS provides solar wind plasma and magnetic field measurements. We use ARTEMIS P1 (formerly THEMIS B) as a solar wind monitor. We also use survey (~4.5 s time resolution) plasma data from the Fast Plasma Investigation (FPI) instrument (Pollock et al., 2016), the DC magnetic field at resolution up to 62.5 ms (survey data) from the Fluxgate Magnetometers (FGM), and the DC electric field with a resolution of 1 ms from the Electron Drift Instrument (EDI) on MMS (Russell et al., 2014; Torbert et al., 2014).

Figure 1 shows projections of ARTEMIS P1, P2, THEMIS A, THEMIS D, and MMS3 spacecraft locations onto the X-Y and X-Z planes from 08:00 UT to 09:00 UT on 28 December 2019 together with the modeled bow shock (Fairfield, 1971) and magnetopause (Shue et al., 1997) locations for the prevailing solar wind conditions. During this time interval, two ARTEMIS spacecraft were far upstream from the bow shock, THEMIS D was in the dawnside foreshock, THEMIS A and MMS were in the dawnside and duskside magnetosheath, respectively.

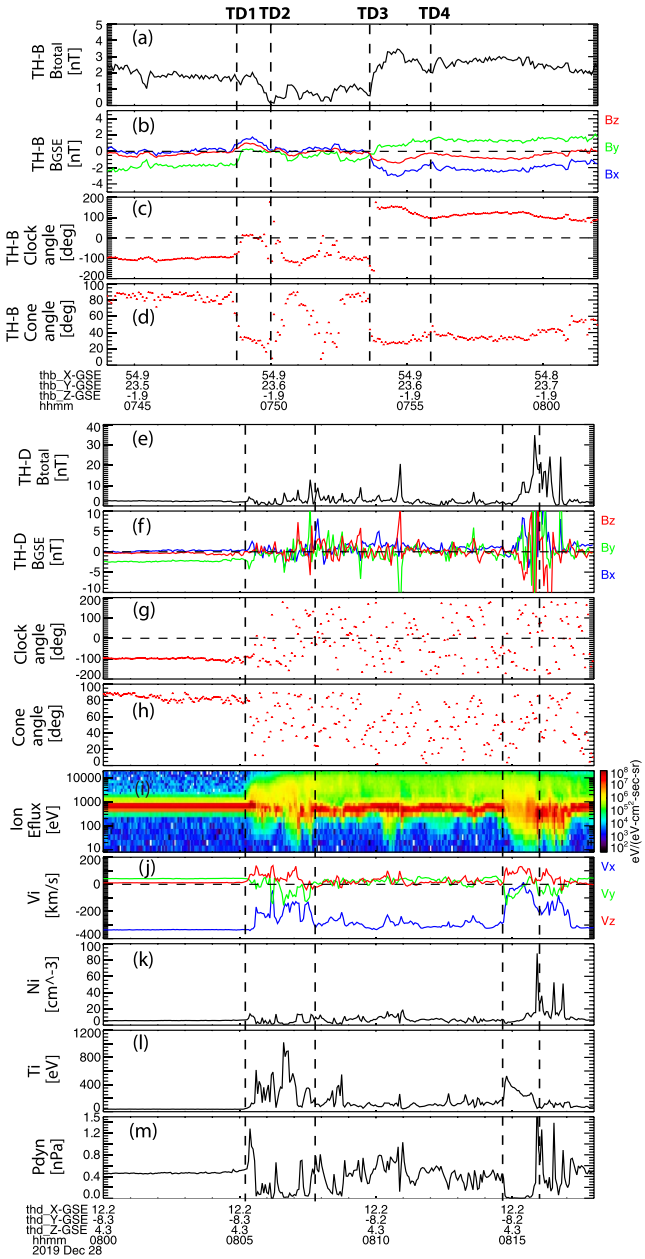

Figure 2. An overview of the foreshock transient event observed on 28 December 2019. From top to bottom: (a–d) Interplanetary magnetic field data from the ARTEMIS P1. (e) The magnetic field strength, (f) components of the magnetic field in GSE coordinate system, (g) magnetic field clock angles, (h) cone angles, (i) plasma ion spectrum, (j) components of plasma flow, (k) ion density, (l) ion temperature, and (m) dynamic pressure. Note that the ARTEMIS P1 data is time shifted by 16 min to be compared with the THEMIS D data. The four discontinuities were selected and were indicated by the vertical lines (TD1, TD2, TD3, and TD4).

Figures 2a–2d show ARTEMIS P1 observations in the pristine solar wind from 07:44 UT to 08:02 UT and Figures 2e–2m show an overview plot of THEMIS D observations in the ion foreshock from 08:00 UT to 08:18 UT on 28 December 2019. THEMIS D entered the foreshock at 08:05 UT and observed a foreshock transient exhibiting strong magnetic field strength fluctuations, enhanced heating, deflected and decreased velocity, and small depressions in density and the magnitude of magnetic field from 08:05:10 UT to 08:07:50 UT. There are two additional foreshock transients observed from 08:14:40 UT to 08:17:10 UT. The two foreshock transients were merging each other and exhibited greatly decelerated and deflected anti-sunward flows, increase in temperature, and depressed plasma density in the core region and the magnetic field strength bounded by one compressional boundary (trailing edge) from 08:14:40 UT to 08:15:50 UT.

Four discontinuities observed by ARTEMIS P1 are associated with THEMIS D entering the foreshock and observing a series of foreshock transients. Vertical dashed lines indicate these four discontinuities (TD1, TD2, TD3, and TD4). We apply a 16 min time shift to all data from ARTEMIS P1 to account for the propagation delay of the first discontinuity to THEMIS D (TH-D). The time delay between ARTEMIS P1 and THEMIS D was calculated using the separation between the two spacecraft and the propagation velocity of the solar wind discontinuity. The first discontinuity observed by ARTEMIS P1 resulted in THEMIS D entering the foreshock. The foreshock transient was confined by the first and second discontinuities. The third and the forth discontinuities also generated foreshock transients at THEMIS D. The propagation delays for the third and the forth discontinuities differ from that for the first discontinuity since the normal directions for the four discontinuities are very different. The propagation time delays for the third and the forth discontinuity normals are about 23 and 24 min, respectively. We employ the 3-D global hybrid simulation model to simulate the interaction of these four discontinuities with the bow shock, magnetosheath, and magnetopause and compare each phenomena observed by THEMIS and MMS spacecraft with the simulation results.

3. Simulation Model and Setup

The 3-D global hybrid code, ANGIE3D (Lin et al., 2014, 2017), is used in this study. In the simulation model, ions are treated as discrete, fully kinetic particles, and the electrons are treated as a massless fluid. Quasi charge neutrality is assumed. The simulation domain includes in the GSM coordinate system x = +30 R_E on the dayside to x = −60 R_E on the night side, y = −35 R_E to +35 R_E in the dawn/dusk direction, and z = −35 R_E to +35 R_E in the north-south direction. An inner boundary is assumed at the geocentric distance of r = ∼3 R_E that couples to the ionosphere along the dipole magnetic field. The ionospheric Poisson's equation is solved with a uniform Pedersen conductance Σ_P = 5 S and a Hall conductance Σ_H = 10 S. In addition to the particle ions, a cold ion fluid has been assumed to dominate the inner magnetosphere for r < 6 R_E (Swift, 1996). Nonuniform cell grids are used, with the grid size around the bow shock, magnetosheath, magnetopause, and the cusp smaller than in other places. In the present study, the solar wind ion inertial length d_{i0} is chosen to be 0.06 R_E, 4 times larger than the realistic value. The cell dimensions are $n_x \times n_y \times n_z = 920 \times 794 \times 450$. A total of $\sim 10^{10-11}$ particles are used.

The simulation starts from a uniform IMF of B_0 = (0, −1.9, −0.42) nT, solar wind velocity of V_0 = (−345, 0, 0) km/s, ion density N_0 = 5/c. c., and ion temperature T_{i0} = 10 eV. The bow shock and magnetosphere form self-consistently by the interaction between the solar wind and the geomagnetic field. The parameters defining the four

Table 1
Solar Wind and IMF Parameters for the 28 December 2019 ARTEMIS P1 Observations Employed in the 3-D Global Hybrid Simulation Run

Discontinuity	TD1	TD2	TD3	TD4
B_{up} (nT)	(0.23, −1.71, −0.24)	(1.5, 0.14, 0.87)	(0.05, −1.05, −0.21)	(−2.84, 0.70, −1.31)
B_{dn} (nT)	(1.5, 0.14, 0.87)	(0.05, −1.05, −0.21)	(−2.84, 0.70, −1.31)	(−2.14, 1.41, −0.57)
V_{up} (km/s)	(−344.0, 10.4, 7.9)	(−341.6, 14.2, 9.8)	(−341.7, 16.7, 11.0)	(−350.4, 21.4, 7.5)
V_{dn} (km/s)	(−341.6, 14.2, 9.8)	(−341.7, 16.7, 11.0)	(−350.4, 21.4, 7.5)	(−357.5, 21.8, 4.9)
Ni_{up} (cm^{-3})	5.81	5.80	5.97	4.58
Ni_{dn} (cm^{-3})	5.80	5.97	4.58	5.15
Ti_{up} (eV)	14.8	14.4	14.5	14.2
Ti_{dn} (eV)	14.4	14.5	14.2	14.8
E_{up} (mV/m)	(−0.01, 0.08, −0.59)	(−0.01, −0.3, 0.07)	(−0.01, 0.07, −0.36)	(0.03, 0.48, 0.18)
E_{dn} (mV/m)	(−0.01, −0.3, 0.07)	(−0.01, 0.07, −0.36)	(0.03, 0.48, 0.18)	(0.02, 0.21, 0.46)
n_{TD}	(−0.48, −0.18, 0.86)	(0.48, 0.19, −0.86)	(−0.45, −0.20, 0.87)	(−0.46, −0.38, 0.80)

discontinuities are shown in Table 1, in which B, V, N_i, and T_i are the magnetic field, ion velocity, ion density and ion temperature across the TDs, while n_{TD} is the TD's normal direction. Figure 3 shows contours of the magnetic field strength in logarithm scale in the noon meridian and equatorial planes at t = 64 min and t = 89 min. The lines of different colors indicate the magnetic field lines at different regions. The fourth TD (TD4) arrives the domain at a later time so that all four TDs are not in the one domain at the same time.

4. Solar Wind Conditions

Figure 4(right) displays the magnetic field and plasma measurements observed by ARTEMIS P1 from 07:32 UT to 08:02 UT on 28 December 2019. Figure 4(left) depicts time variations of the magnetic field strength, three components of the magnetic field, IMF clock angle, cone angle, solar wind velocity, ion density, total ion temperature, and three components of the electric field at a fixed position (X, Y, Z) = (25.0, 23.7, −2.0) R_E. ARTEMIS P1 was located in the pristine solar wind at (X, Y, Z) = (54.8, 23.7, −1.9) R_E. The four discontinuities are denoted by the vertical dashed lines.

Table 1 lists the parameters upstream and downstream of the four discontinuities. There are changes in density, temperature and magnetic field magnitude across the discontinuities. There are magnetic field fluctuations

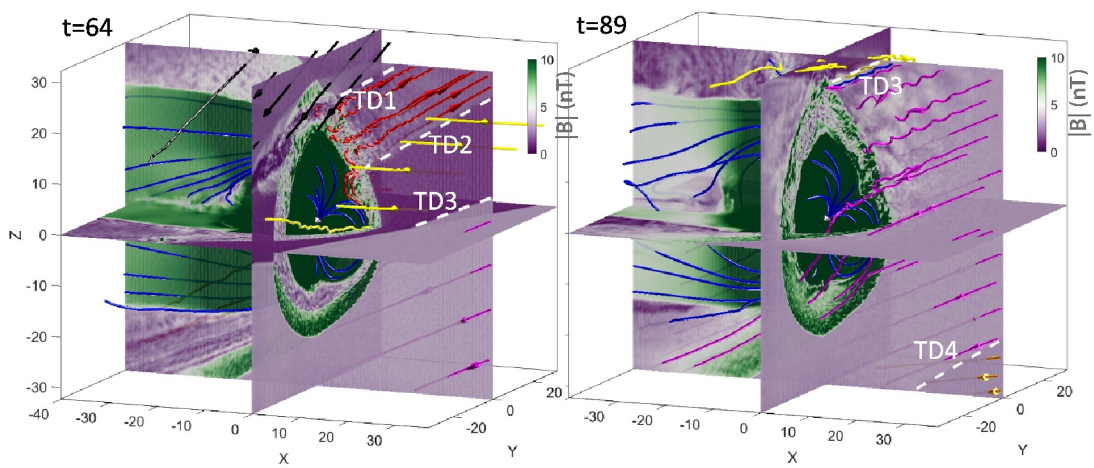

Figure 3. Simulation results of magnetic field at t = 64 min and t = 89 min. The white dashed lines represent the intersection between the TD planes and Sun-Earth meridian plane for TD1, 2, 3, and 4, respectively. The colored solid lines represent 3-D magnetic field lines at different regions (black: downstream of TD1; red: upstream of TD1; yellow: upstream of TD2; purple: upstream of TD3; orange: upstream of TD4; blue: magnetosphere). Contours show magnetic field strength in units of nT.

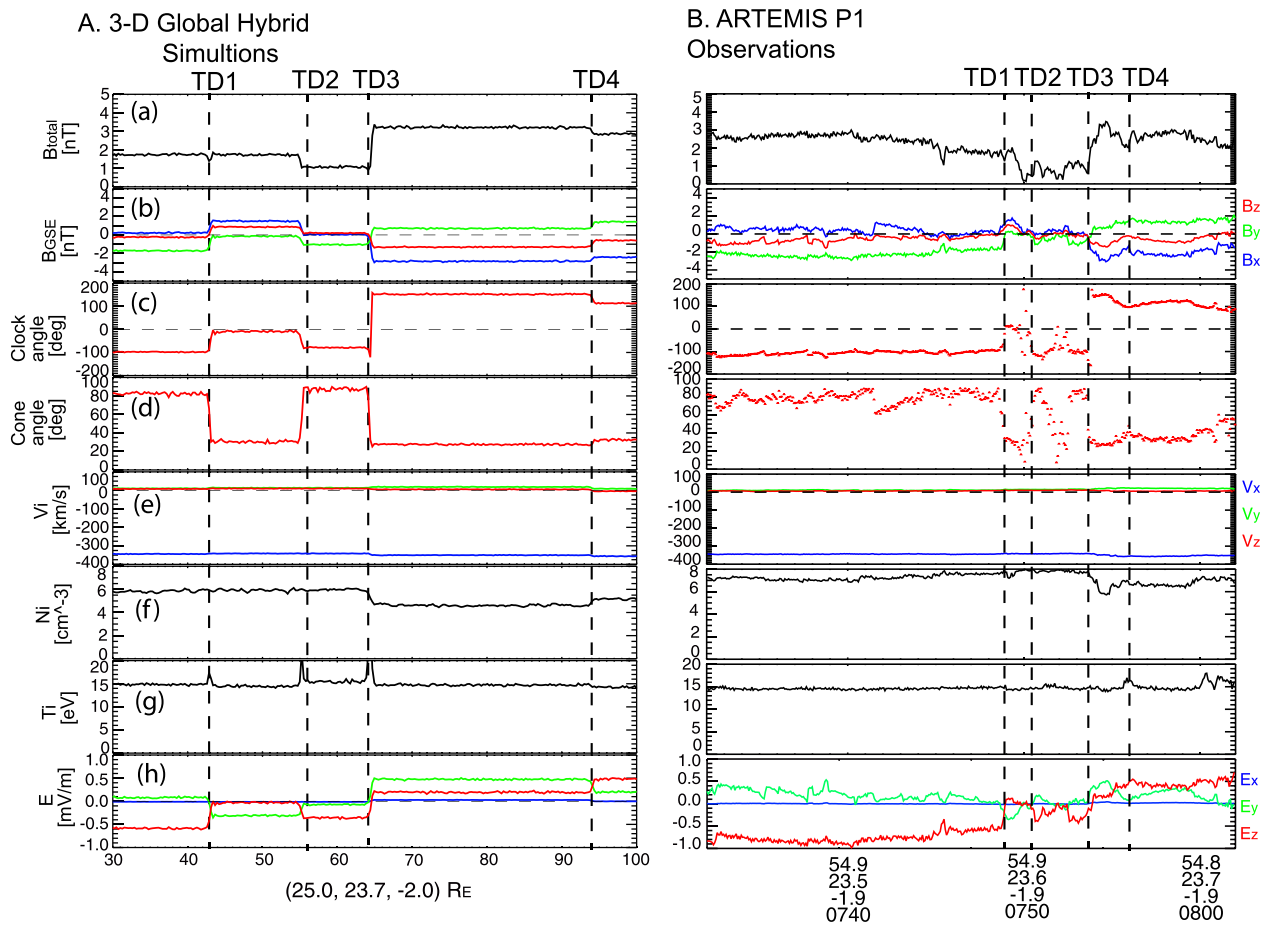

Figure 4. (left) Virtual spacecraft and (right) ARTEMIS P1 data from the position at (25.0, 23.7, −2.0) R_E and ∼(54.8, 23.7, −1.9) R_E, respectively. From top to bottom for both 3-D global hybrid simulation and ARTEMIS P1: (a) magnetic field strength, (b) magnetic field components, (c) magnetic field clock angles, (d) cone angles, (e) ion bulk flow velocities, (f) number density, (g) ion temperature, and (h) electric field components. The four vertical dashed lines indicate the four discontinuities.

between TD1 and TD3 in the observations. The IMF clock angle changes to 0° right after the TD1 and goes back to −100° right after the TD2. The magnetic field orientations downstream of TD1 and TD2 in the simulation and observation are quite different. The magnetic field fluctuations observed between TD1 and TD3 are stronger than those in the simulation. The values of the magnetic field intensity and the density from ARTEMIS P1 are averaged between the discontinuities and are used for the simulation initial conditions. If we set perturbations in the simulation, it would lead to inconsistent input and result in unexpected structures around boundary.

We tested the Walén relation (Phan et al., 2004) and found that the vector changes in the magnetic fields and plasma velocities before and after the discontinuities are not correlated each other. The negative Walén test result further supports TD instead of RD. We estimated discontinuity normals (**n**) using minimum variance analysis (MVA) (Sonnerup & Cahill, 1967) and the cross-product method on observations before (upstream) and after (downstream) the discontinuities ($\mathbf{n} = (\mathbf{B}_u \times \mathbf{B}_d)/|\mathbf{B}_u \times \mathbf{B}_d|$). The normal directions for the discontinuities obtained from the MVA is consistent with that from the cross-product method. The changes in each parameter across the four discontinuities are consistent with the observations. The time separations between the discontinuities are longer than those in the observations. If we place the discontinuities according to the realistic timing, some discontinuities would see their intersection at the boundary because their fronts are highly oblique relative to each other. It is difficult to model such boundary conditions correctly. To this end, the simulation increases the time separation between the TDs in order to avoid intersection of TD planes.

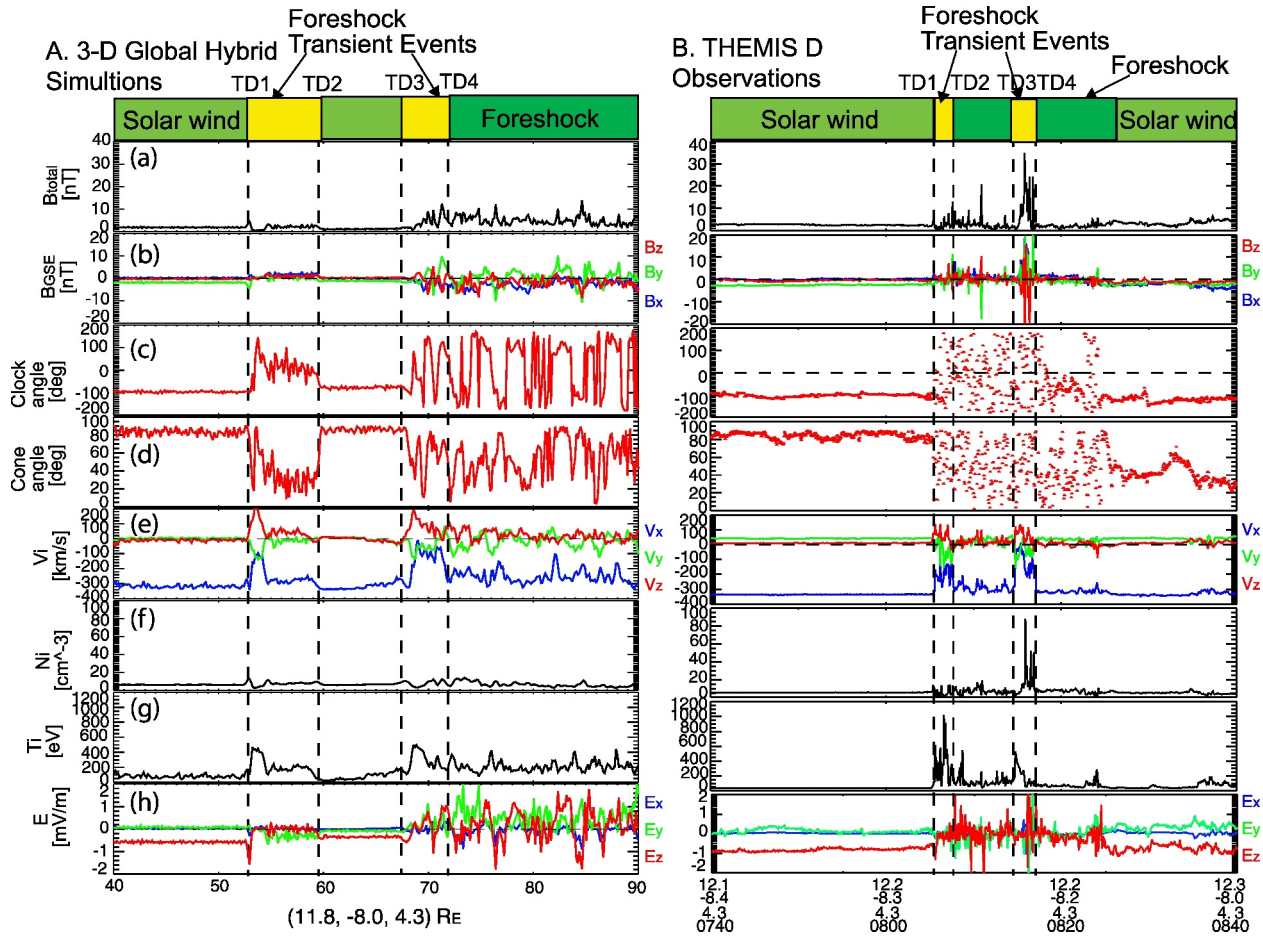

Figure 5. Magnetic field and plasma parameters for a region in the foreshock where a foreshock transient event was present. Magnetic field and plasma data in the same format as Figure 4. The four vertical dashed lines are associated with the four solar wind discontinuities. Both simulation results and the THEMIS D observations show the foreshock transients which are HFA-like structures and are associated with the first and the third discontinuities.

5. Results and Discussion

Here we compare THEMIS D, A, and MMS plasma and magnetic field observations of foreshock transients, a magnetosheath cavity-like structure, and a brief magnetopause crossing with the predictions of the hybrid code model.

5.1. Comparison of Foreshock Transients: HFA-Like Structures

We compare THEMIS D plasma and magnetic field observations of the foreshock transient with the results of the 3-D global hybrid simulations shown in Figure 5. Figure 5 presents plasma and magnetic field measurements at a fixed location in the dawn foreshock (X, Y, Z) = (11.8, −8.3, 4.3) R_E in the simulation (left column) and THEMIS D observations from 07:40 UT to 08:40 UT on 28 December 2019 at (X, Y, Z) = ∼(12.2, −8.2, 4.3) R_E (right column). Four vertical dashed lines indicate arrival times for the four discontinuities in the foreshock. The overall structures across the dashed lines in the simulation are remarkably similar to those in the observations.

The first discontinuity (TD1) causes the foreshock to move to the locations of the virtual spacecraft and THEMIS D. Magnetic field strength fluctuations are enhanced in the foreshock. The amplitude of the magnetic field strength (∼5 nT) in the observations is 10 times larger than that (∼0.6 nT) in the simulation after TD1. In the observations, there is the first foreshock transient (FT1) which can be associated with the first and the second discontinuities (08:05:30 UT–08:07:50 UT). Its core region exhibits strong heating, strong deflection of the velocity, and small depressions in density and the magnitude of magnetic field. In the simulation result, the velocity and the density decrease and the temperature increases during 2 min after the

Table 2
Properties of the Two Foreshock Transients (FT1 and FT2), a Cavity-Like Structure in the Magnetosheath (MSH), and a Magnetopause Crossing (MSP) Detected by the Virtual Spacecraft (SIM) and by the Multi-Spacecraft (OBS)

	FT1				FT2				MSH				MSP			
	$\frac{\lvert B_{min}\rvert}{\lvert B_{sw}\rvert}$	$\frac{V_{x,min}}{V_{x,sw}}$	$\frac{N_{min}}{N_{sw}}$	$\frac{T_{max}}{T_{sw}}$	$\frac{\lvert B_{min}\rvert}{\lvert B_{sw}\rvert}$	$\frac{V_{x,min}}{V_{x,sw}}$	$\frac{N_{min}}{N_{sw}}$	$\frac{T_{max}}{T_{sw}}$	$\frac{\lvert B_{min}\rvert}{\lvert B_{msh}\rvert}$	$\frac{V_{x,min}}{V_{x,msh}}$	$\frac{N_{min}}{N_{msh}}$	$\frac{T_{max}}{T_{msh}}$	$\frac{\lvert B_{max}\rvert}{\lvert B_{msh}\rvert}$	$\frac{V_{x,min}}{V_{x,msh}}$	$\frac{N_{min}}{N_{msh}}$	$\frac{T_{max}}{T_{msh}}$
OBS	0.4	0.16	0.15	20.0	0.12	−0.07	0.33	4.08	0.02	−0.63	0.67	0.75	2.3	−1.29	0.02	7.5
SIM	0.2	0.29	0.46	4.5	0.45	0.0	0.54	5.0	0.06	−0.2	0.15	2.72	3.5	−0.4	0.2	0.6

Note. The magnitudes of depletions of magnetic field strength, X-component of ion velocity, and ion density, plasma heating inside the events are listed.

first discontinuity arrived at ∼53 min. The values of the depressed magnetic field strength (B_{min}/B_{sw}) and plasma density depletions (N_{min}/N_{sw}) and flow deflections ($V_{X,min}/V_{X,sw}$) and heated plasma (T_{max}/T_{sw}) in the core of the transient event for both simulations (SIM) and observations (OBS) are listed in Table 2. There are plateaus of magnetic field strength, velocity, density, and temperature before the second discontinuity arriving. The plateaus from the simulation results may be due to the different solar wind conditions between the simulation and the observations. There are more than four discontinuities in the observations, making the conditions not exactly identical to the simulations.

The next consecutive foreshock transients which are related to the third (TD3) and the forth discontinuities (TD4) are shown in both simulations and observations. The third discontinuity is associated with a fully developed foreshock transient (FT2) with a core region exhibiting greatly decelerated and deflected anti-sunward flows, increase in temperature, and depressed plasma density. In the observations, the magnetic field strength and the number density are bounded by one compressional boundary (trailing edge) from 08:14:40 UT to 08:08:15:50 UT. Both magnetic field strength and number density show less compression on the trailing edge in the simulations. The properties of the second foreshock transient (FT2) for the simulations and the observations are shown in Table 2. Different from the simulations, there can be another foreshock transient exhibiting decelerated and deflected flows in the observations (08:16:00 UT–08:17:10 UT). However, there are no significant changes in density, magnetic field strength, temperature across the third transient. This indicates that the third foreshock transient has not fully developed. The observations showed that the third transient was merging with the second one so that it is difficult to identify the characteristics of the third one.

5.2. Comparison of Magnetosheath Cavity-Like Structure

The density perturbations of foreshock transients correspond to dynamic pressure perturbations. As the perturbations propagate into the magnetosheath, they can cause magnetopause distortion. The resulting magnetosheath motion and the impacts on the dayside magnetopause have been observed and simulated (Archer et al., 2014; Lin, 2002; Lin & Wang, 2005; Omidi et al., 2016; Shi et al., 2013, 2021; Sibeck et al., 1999, 2000, 2021; C.-P. Wang et al., 2020).

Figure 6(right) shows the MMS observations of magnetic field perturbations possibly resulting from the solar wind discontinuities and/or foreshock transients observed in the foreshock. The MMS spacecraft were in the magnetosheath from 08:00 UT to 08:30 UT and behind the quasi-parallel magnetosheath at 08:08 UT. Diamagnetic cavities in the foreshock and magnetosheath cavities characterized by depressed densities and magnetic fields and accompanied by enhanced fluxes of energetic particles have been observed (Katırcıoğlu et al., 2009; Sibeck et al., 2001, 2002, 2021). A magnetosheath cavity-like structure was observed downstream from the foreshock from 08:18:50 UT to 08:20:40 UT. The magnetic field strength decrease approximately 50% of the ambient magnetosheath magnetic field. This decrease was bounded by a stronger compression at 08:20:40 UT–08:21:40 UT, which is clear in the B_Y and B_Z field components. The density slowly decreased during the magnetic field depression and a large depression at least 40% appeared in the strong magnetic field compression 08:20:40 UT–08:22:00 UT. There is a velocity deflection, even sunward-moving flow (positive V_X), inside the cavity and the total temperature decreases during the interval. The energy spectra observed by the EIS instruments (not shown in Figure 6, right) indicate that enhanced fluxes of energetic particles were already present in the quasi-parallel magnetosheath from 08:08 UT. This is not consistent with the previous results of high energy particles within the cavities from Sibeck et al. (2002) and Katırcıoğlu et al. (2009).

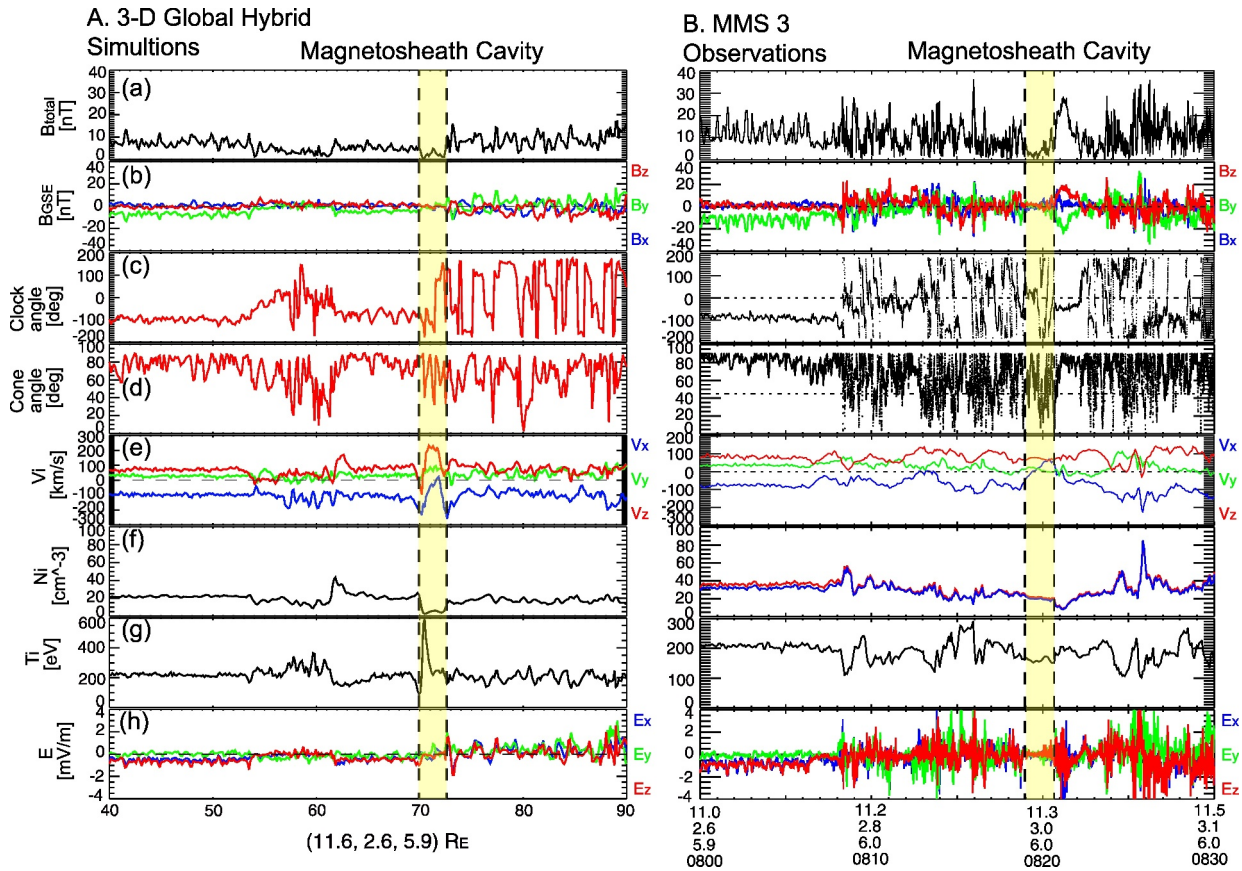

Figure 6. (left) Magnetic field and plasma parameters for a region in the magnetosheath where a magnetosheath cavity which can be an impact of the foreshock transient was detected at (11.6, 2.6, 5.9) R_E in the simulation and at MMS spacecraft position ~(11.3, 3.0, 6.0) R_E. Magnetic field and plasma data in the same format as Figure 4. The region from 08:19 UT to 08:20 UT mark the magnetosheath cavity-like structure. Magnetic field and plasma data in the same format as Figure 4.

Figure 6(left) shows the temporal profiles of magnetic field and plasma parameters that were observed by a simulated virtual satellite in the magnetosheath at (X, Y, Z) = (11.6, 2.6, 5.9) R_E. The virtual satellite observed weak magnetic field strength and density and a decelerated flow (positive V_X) inside the structure from 70 to 73 min. These features are qualitatively similar to the observed magnetosheath cavity-like structure shown in Figure 6(right). The quantitative comparison of properties of the structures (MSH) between simulations and observations is listed in Table 2. However, there are relatively weaker magnetic field compression surrounded by the cavity and stronger depression in density and enhancement in temperature, which are different from the observations.

5.3. Magnetopause Crossing

Figure 7 compares observations of a magnetopause crossing (a yellow shaded region) which can be associated with the arrival of the solar wind discontinuity and/or a foreshock transient with a magnetopause distortion seen in the simulations. THEMIS A was in the magnetosheath located at ~(10.2, −5.9, 4.4) R_E in GSE coordinates from 08:00 UT to 08:30 UT. As shown in Figure 7(right), THEMIS A observations show that the dayside magnetopause and magnetosphere protrude outward from 08:23:30 UT to 08:24:10 UT. Similar to the THEMIS A observations, Figure 7(left) shows a simulated magnetopause crossing (a yellow shaded region) in the magnetosheath at location (X, Y, Z) = (8.6, −6.1, 4.5) R_E.

The outward protruding magnetosphere is indicated by the plasma with relatively higher magnetic field strength (Figures 7a and 7b) and strongly deflected velocity (sunward flows, Figure 7e) and lower density (Figure 7f) compared to the surrounding magnetosheath plasma. However, the ion temperature enhancement which is a characteristic feature of the magnetosphere did not appear in the simulations. The detailed comparison of the

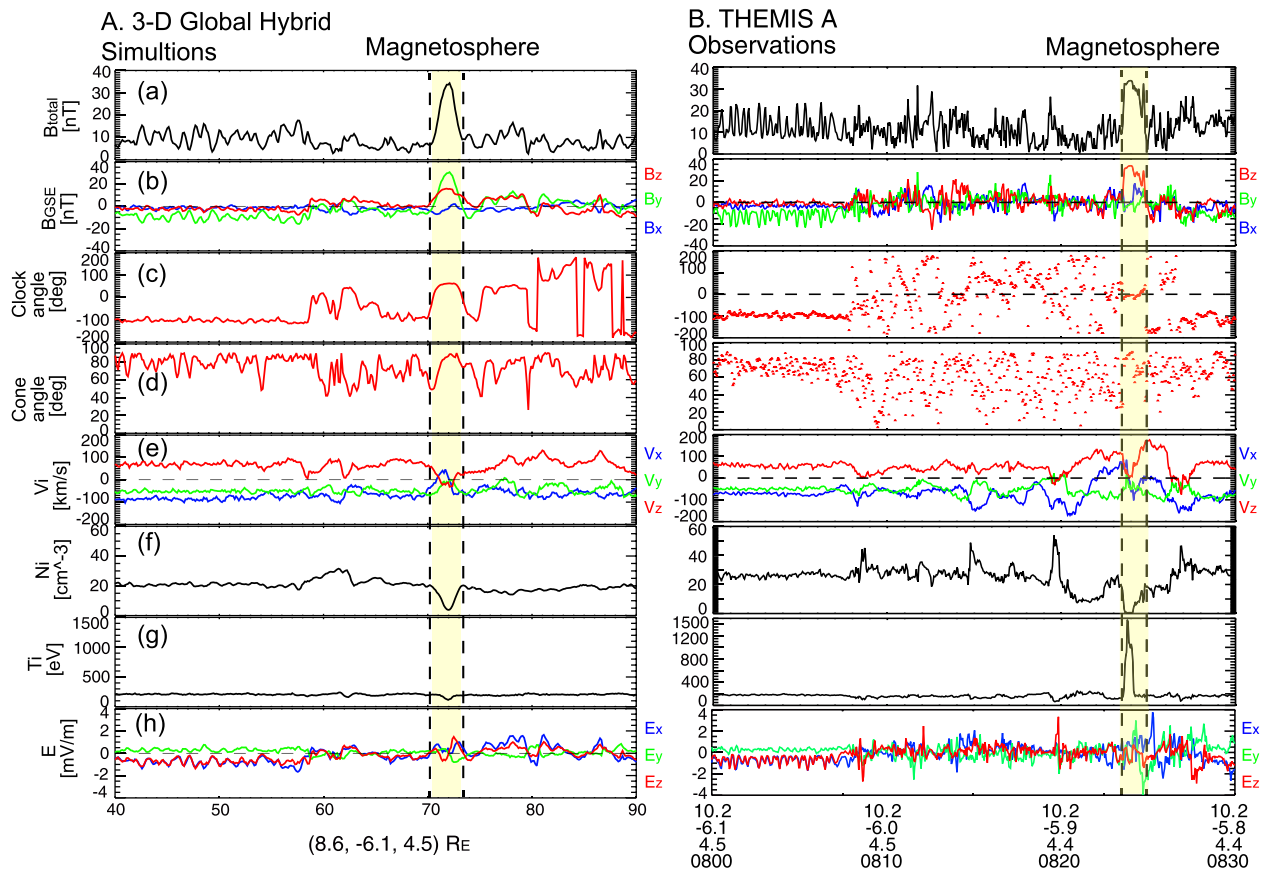

Figure 7. (left) Time series of the virtual spacecraft from the position (8.6, −6.1, 4.5) R_E and (right) magnetosheath observations from THEMIS A with the spacecraft locations at (10.2, −5.9, 4.4) R_E in GSE noted. The yellow shaded regions indicate an entry of magnetosphere. Magnetic field and plasma data in the same format as Figure 4.

properties of the magnetopause crossing between the simulations and observations is listed in Table 2. The observed magnetic field strength, deflected velocity, and depression in density during the magnetopause crossing are remarkably consistent with the simulation results.

6. Summary and Conclusions

We have presented the first detailed comparison of multi-spacecraft observations of foreshock transients and their magnetospheric responses with results from 3-D global hybrid simulations. ARTEMIS P1 observed a series of discontinuities in the region far upstream from the bow shock from 0740 UT to 0800 UT on 28 December 2019. The THEMIS D observations show several foreshock transients in the foreshock which are associated with the solar wind discontinuities and its core regions exhibit strong heating, strong deflection of the velocity, and small depression in density and magnetic field strength. The MMS spacecraft located in the magnetosheath observed a cavity-like structure exhibiting a decrease in magnetic field strength and highly deflected velocity downstream from the foreshock. THEMIS A was in the dawnside magnetosheath and observed an outward protruding magnetosphere. THEMIS A observed higher magnetic field strengths and strongly deflected velocities during the brief magnetopause crossing. The spacecraft observations of the magnetosheath cavity-like structure and magnetopause crossing can be due to the discontinuities and the foreshock transients in the foreshock which can cause magnetopause distortion resulting from the perturbations in dynamic pressure. We simulated the response to the four discontinuities. The simulation predicted the occurrence of foreshock transients, a cavity-like structure in the magnetosheath, and a brief magnetopause crossing as observed by the multi-spacecraft array. The detailed comparisons of the magnetic field and plasma profiles between the observations and the simulations are listed in Table 2. The simulation parameters are simplified as compared with observations, which contains many smaller

amplitude structures. But the overall characteristics of the each observed structures remarkably agree well with the simulation results.

Data Availability Statement

The MMS data set is available online (MMS Science Data Center at https://lasp.colorado.edu/mms/sdc/public/). The entire THEMIS, ARTEMIS data and THEMIS software (SPEDAS) are available by downloading http://themis.ssl.berkeley.edu. The simulation data can be found in X. Wang et al. (2023).

Acknowledgments
We acknowledge NASA contract NAS5-02099 for use of data from the THEMIS Mission. Specifically, we thank K. H. Glassmeier, U. Auster and W. Baumjohann for the use of FGM data provided under the lead of the Technical University of Braunschweig and with financial support through the German Ministry for Economy and Technology and the German Center for Aviation and Space (DLR) under contract 50 OC 0302 and C. W. Carlson and J. P. McFadden for use of ESA data. We would like to thank the FGM, ESA, and FPI instrument teams of the THEMIS, ARTEMIS, and MMS mission for the successful spacecraft operation and for providing plasma and magnetic field data. This study benefited from discussions within the International Space Science Institute (ISSI) team on "Impact of Upstream Mesoscale Transients on the Near-Earth Environment." Some of the work conducted at NASA/GSFC was supported by the MMS project. This work at Auburn University is supported by NASA Grants NASA-80NSSC20K1322, 80NSSC23K0086, 80NSSC22K1012, and the NSF Grants AGS-2247759 and AGS-2224109. Computer resources for the simulations were provided by NASA Advanced Supercomputing (NAS) Division.

References

Angelopoulos, V. (2008). The THEMIS mission. *Space Science Reviews*, *141*(1–4), 5–34. https://doi.org/10.1007/s11214-008-9336-1

Angelopoulos, V. (2011). The ARTEMIS mission. *Space Science Reviews*, *165*(1–4), 3–25. https://doi.org/10.1007/s11214-010-9687-2

Archer, M. O., Turner, D. L., Eastwood, J. P., Horbury, T. S., & Schwartz, S. J. (2014). The role of pressure gradients in driving sunward magnetosheath flows and magnetopause motion. *Journal of Geophysical Research: Space Physics*, *119*(10), 8117–8125. https://doi.org/10.1002/2014JA020342

Archer, M. O., Turner, D. L., Eastwood, J. P., Schwartz, S. J., & Horbury, T. S. (2015). Global impacts of a foreshock bubble: Magnetosheath, magnetopause and ground-based observations. *Planetary and Space Science*, *106*, 56–66. https://doi.org/10.1016/j.pss.2014.11.026

Auster, H. U., Glassmeier, K. H., Magnes, W., Aydogar, O., Baumjohann, W., Constantinescu, D., et al. (2008). The THEMIS fluxgate magnetometer. *Space Science Reviews*, *141*(1–4), 235–264. https://doi.org/10.1007/s11214-008-9365-9

Blanco-Cano, X., Kajdič, P., Omidi, N., & Russell, C. T. (2011). Foreshock cavitons for different interplanetary magnetic field geometries: Simulations and observations. *Journal of Geophysical Research*, *116*(A9), A09101. https://doi.org/10.1029/2010JA016413

Bonnell, J. W., Mozer, F. S., Delory, G. T., Hull, A. J., Ergun, R. E., Cully, C. M., et al. (2008). The electric field instrument (EFI) for THEMIS. *Space Science Reviews*, *141*(1–4), 303–341. https://doi.org/10.1007/s11214-008-9469-2

Burch, J. L., Moore, T. E., Torbert, R. B., & Giles, B. L. (2016). Magnetospheric multiscale overview and science objectives. *Space Science Reviews*, *199*(1–4), 5–21. https://doi.org/10.1007/s11214-015-0164-9

Eastwood, J. P., Lucek, E. A., Mazelle, C., Meziane, K., Narita, Y., Pickett, J., & Treumann, R. A. (2005). The foreshock. *Space Science Reviews*, *118*(1–4), 41–94. https://doi.org/10.1007/s11214-005-3824-3

Fairfield, D. H. (1971). Average and unusual locations of the Earth's magnetopause and bow shock. *Journal of Geophysical Research*, *76*(28), 6700–6716. https://doi.org/10.1029/ja076i028p06700

Guo, Z., Lin, Y., Wang, X., Vines, S. K., Lee, S. H., & Chen, Y. (2020). Magnetopause reconnection as influenced by the dipole tilt under southward IMF conditions: Hybrid simulation and MMS observation. *Journal of Geophysical Research: Space Physics*, *125*(9), e2020JA027795. https://doi.org/10.1029/2020JA027795

Katırcıoğlu, F. T., Kaymaz, Z., Sibeck, D. G., & Dandouras, I. (2009). Magnetosheath cavities: Case studies using cluster observations. *Annales Geophysicae*, *27*(10), 3765–3780. https://doi.org/10.5194/angeo-27-3765-2009

Lee, S. H., Sibeck, D. G., Omidi, N., Silveira, M. V. D., Giles, B. L., Torbert, R. B., et al. (2021). Comparison of MMS observations of foreshock bubbles with a global hybrid simulation. *Journal of Geophysical Research: Space Physics*, *126*(7), e28848. https://doi.org/10.1029/2020JA028848

Lin, Y. (1997). Generation of anomalous flows near the bow shock by its interaction with interplanetary discontinuities. *Journal of Geophysical Research*, *102*(A11), 24265–24281. https://doi.org/10.1029/97JA01989

Lin, Y. (2002). Global hybrid simulation of hot flow anomalies near the bow shock and in the magnetosheath. *Planetary and Space Science*, *50*(5–6), 577–591. https://doi.org/10.1016/s0032-0633(02)00037-5

Lin, Y. (2003). Global-scale simulation of foreshock structures at the quasi-parallel bow shock. *Journal of Geophysical Research*, *108*(A11), 1390. https://doi.org/10.1029/2003JA009991

Lin, Y., Wang, X., Sibeck, D. G., Wang, C.-P., & Lee, S.-H. (2022). Global asymmetries of hot flow anomalies. *Geophysical Research Letters*, *49*(4), e2021GL096970. https://doi.org/10.1029/2021GL096970

Lin, Y., & Wang, X. Y. (2005). Three-dimensional global hybrid simulation of dayside dynamics associated with the quasi-parallel bow shock. *Journal of Geophysical Research*, *110*(A12), A12216. https://doi.org/10.1029/2005JA011243

Lin, Y., Wang, X. Y., Lu, S., Perez, J. D., & Lu, Q. (2014). Investigation of storm time magnetotail and ion injection using three-dimensional global hybrid simulation. *Journal of Geophysical Research: Space Physics*, *119*(9), 7413–7432. https://doi.org/10.1002/2014JA020005

Lin, Y., Wing, S., Johnson, J. R., Wang, X. Y., Perez, J. D., & Cheng, L. (2017). Formation and transport of entropy structures in the magnetotail simulated with a 3-D global hybrid code. *Geophysical Research Letters*, *44*(12), 5892–5899. https://doi.org/10.1002/2017GL073957

McFadden, J. P., Carlson, C. W., Larson, D., Ludlam, M., Abiad, R., Elliott, B., et al. (2008). The THEMIS ESA plasma instrument and in-flight calibration. *Space Science Reviews*, *141*(1–4), 277–302. https://doi.org/10.1007/s11214-008-9440-2

Omidi, N., Berchem, J., Sibeck, D., & Zhang, H. (2016). Impacts of spontaneous hot flow anomalies on the magnetosheath and magnetopause. *Journal of Geophysical Research: Space Physics*, *121*(4), 3155–3169. https://doi.org/10.1002/2015JA022170

Omidi, N., Eastwood, J. P., & Sibeck, D. G. (2010). Foreshock bubbles and their global magnetospheric impacts. *Journal of Geophysical Research*, *115*(A6), A06204. https://doi.org/10.1029/2009JA014828

Omidi, N., Sibeck, D., Blanco-Cano, X., Rojas-Castillo, D., Turner, D., Zhang, H., & Kajdič, P. (2013). Dynamics of the foreshock compressional boundary and its connection to foreshock cavities. *Journal of Geophysical Research: Space Physics*, *118*(2), 823–831. https://doi.org/10.1002/jgra.50146

Omidi, N., & Sibeck, D. G. (2007). Formation of hot flow anomalies and solitary shocks. *Journal of Geophysical Research*, *112*(A1), A01203. https://doi.org/10.1029/2006JA011663

Phan, T., Dunlop, M., Paschmann, G., Klecker, B., Bosqued, J., Rème, H., et al. (2004). Cluster observations of continuous reconnection at the magnetopause under steady interplanetary magnetic field conditions. *Annales Geophysicae*, *22*(7), 2355–2367. https://doi.org/10.5194/angeo-22-2355-2004

Pollock, C., Blake, J. B., Baker, D. N., Clemmons, J. H., Reeves, G. D., Spence, H. E., et al. (2016). Fast plasma investigation for magnetospheric multiscale. *Space Science Reviews*, *199*(1–4), 331–406. https://doi.org/10.1007/s11214-016-0245-4

Russell, C. T., Anderson, B. J., Baumjohann, W., Bromund, K. R., Dearborn, D., Fischer, D., et al. (2014). The magnetospheric multiscale magnetometers. *Space Science Reviews*, *199*(1–4), 189–256. https://doi.org/10.1007/s11214-014-0057-3

Schwartz, S. J., Chaloner, C. P., Hall, D. S., Christiansen, P. J., Johnstones, A. D., Johnstone, A. D., et al. (1985). An active current sheet in the solar wind. *Nature*, *318*(6043), 269–271. https://doi.org/10.1038/318269a0

Shen, X.-C., Shi, Q., Wang, B., Zhang, H., Hudson, M. K., Nishimura, Y., et al. (2018). Dayside magnetospheric and ionospheric responses to a foreshock transient on 25 June 2008: 1. FLR observed by satellite and ground-based magnetometers. *Journal of Geophysical Research: Space Physics*, *123*(8), 6335–6346. https://doi.org/10.1029/2018JA025349

Shi, F., Lin, Y., & Wang, X. (2013). Global hybrid simulation of mode conversion at the dayside magnetopause. *Journal of Geophysical Research: Space Physics*, *118*(10), 6176–6187. https://doi.org/10.1002/jgra.50587

Shi, F., Lin, Y., Wang, X., Wang, B., & Nishimura, Y. (2021). 3-D global hybrid simulations of magnetospheric response to foreshock processes. *Earth Planets and Space*, *73*(1), 138. https://doi.org/10.1186/s40623-021-01469-2

Shue, J.-H., Chao, J. K., Fu, H. C., Russell, C. T., Song, P., Khurana, K. K., & Singer, H. J. (1997). A new functional form to study the solar wind control of the magnetopause size and shape. *Journal of Geophysical Research*, *102*(A5), 9497–9512. https://doi.org/10.1029/97JA00196

Sibeck, D. G., Decker, R. B., Mitchell, D. G., Lazarus, A. J., Lepping, R. P., & Szabo, A. (2001). Solar wind preconditioning in the flank foreshock: IMP 8 observations. *Journal of Geophysical Research*, *106*(A10), 21675–21688. https://doi.org/10.1029/2000JA000417

Sibeck, D. G., Kudela, K., Lepping, R. P., Lin, R., Nemecek, Z., Nozdrachev, M. N., et al. (2000). Magnetopause motion driven by interplanetary magnetic field variations. *Journal of Geophysical Research*, *105*(A11), 25155–25169. https://doi.org/10.1029/2000JA900109

Sibeck, D. G., Lee, S.-H., Omidi, N., & Angelopoulos, V. (2021). Foreshock cavities: Direct transmission through the bow shock. *Journal of Geophysical Research: Space Physics*, *126*(5), e2021JA029201. https://doi.org/10.1029/2021JA029201

Sibeck, D. G., Omidi, N., Dandouras, I., & Lucek, E. (2008). On the edge of the foreshock: Model-data comparisons. *Annales Geophysicae*, *26*(6), 1539–1544. https://doi.org/10.5194/angeo-26-1539-2008

Sibeck, D. G., Paschmann, G., Treumann, R. A., Fuselier, S. A., Lennartsson, W., Ogilvie, R. L. K. W., et al. (1999). Plasma transfer processes at the magnetopause. In B. Hultqvist, & M. Øieroset (Eds.), *Magnetospheric plasma sources and losses* (pp. 207–283). Kluwer Acade.

Sibeck, D. G., Phan, T. D., Lin, R., Lepping, R. P., & Szabo, A. (2002). Wind observations of foreshock cavities: A case study. *Journal of Geophysical Research*, *107*(A10), 1271. https://doi.org/10.1029/2001JA007539

Sonnerup, B. U. Ö., & Cahill, L. J., Jr. (1967). Magnetopause structure and attitude from Explorer 12 observations. *Journal of Geophysical Research*, *72*(1), 171–183. https://doi.org/10.1029/jz072i001p00171

Swift, D. W. (1996). Use of a hybrid code for global-scale plasma simulation. *Journal of Computational Physics*, *126*(1), 109–121. https://doi.org/10.1006/jcph.1996.0124

Torbert, R. B., Russell, C. T., Magnes, W., Ergun, R. E., Lindqvist, P.-A., LeContel, O., et al. (2014). The FIELDS instrument suite on MMS: Scientific objectives, measurements, and data products. *Space Science Reviews*, *199*(1–4), 105–135. https://doi.org/10.1007/s11214-014-0109-8

Turner, D. L., Eriksson, S., Phan, T. D., Angelopoulos, V., Tu, W., Liu, W., et al. (2011). Multispacecraft observations of a foreshock-induced magnetopause disturbance exhibiting distinct plasma flows and an intense density compression. *Journal of Geophysical Research*, *116*(A4), A04230. https://doi.org/10.1029/2010JA015668

Turner, D. L., Omidi, N., Sibeck, D. G., & Angelopoulos, V. (2013). First observations of foreshock bubbles upstream of Earth's bow shock: Characteristics and comparisons to HFAs. *Journal of Geophysical Research: Space Physics*, *118*(4), 1552–1570. https://doi.org/10.1002/jgra.50198

Wang, B., Nishimura, Y., Hietala, H., Shen, X.-C., Shi, Q., Zhang, H., et al. (2018). Dayside magnetospheric and ionospheric responses to a foreshock transient on 25 June 2008: 2. 2-D evolution based on dayside auroral imaging. *Journal of Geophysical Research: Space Physics*, *123*(8), 6347–6359. https://doi.org/10.1029/2017JA024846

Wang, C.-P., Wang, X., Liu, T. Z., & Lin, Y. (2020). Evolution of a foreshock bubble in the midtail foreshock and impact on the magnetopause: 3-D global hybrid simulation. *Geophysical Research Letters*, *47*(22), e2020GL089844. https://doi.org/10.1029/2020GL089844

Wang, C.-P., Wang, X., Liu, T. Z., & Lin, Y. (2021a). A foreshock bubble driven by an IMF tangential discontinuity: 3D global hybrid simulation. *Geophysical Research Letters*, *48*(9), e2021GL093068. https://doi.org/10.1029/2021GL093068

Wang, C.-P., Wang, X., Liu, T. Z., & Lin, Y. (2021b). Impact of foreshock transients on the flank magnetopause and magnetosphere and the ionosphere. *Frontiers in Astronomy and Space Sciences*, *8*. https://doi.org/10.3389/fspas.2021.751244

Wang, X., Lin, Y., Lee, S. H., & Sibeck, D. G. (2023). Cross-comparison of observations with the predictions of global hybrid simulations for multiple IMF discontinuities impacting the bow shock and magnetosheath [Dataset]. *Figshare*. https://doi.org/10.6084/m9.figshare.24562414.v1

Zhang, H., Sibeck, D. G., Zong, Q. G., Omidi, N., Turner, D., & Clausen, L. B. N. (2013). Spontaneous hot flow anomalies at quasi-parallel shocks: 1. Observations. *Journal of Geophysical Research: Space Physics*, *118*(6), 3357–3363. https://doi.org/10.1002/jgra.50376

Zhang, H., & Zong, Q. (2020). Transient phenomena at the magnetopause and bow shock and their ground signatures. In *Dayside magnetosphere interactions* (pp. 11–37). American Geophysical Union (AGU). https://doi.org/10.1002/9781119509592.ch2

Zhang, H., Zong, Q., Connor, H., Delamere, P., Facskó, G., Han, D., et al. (2022). Dayside transient phenomena and their impact on the magnetosphere and ionosphere. *Space Science Reviews*, *218*(40), 40. https://doi.org/10.1007/s11214-021-00865-0

Zhao, L. L., Zhang, H., & Zong, Q. G. (2017). Global ULF waves generated by a hot flow anomaly. *Geophysical Research Letters*, *44*(11), 5283–5291. https://doi.org/10.1002/2017GL073249